

C. C. Koch
L. H. Smith, Jr.
Mem. ASME

Aircraft Engine Group,
General Electric Co.,
Cincinnati, Ohio

Loss Sources and Magnitudes in Axial-Flow Compressors

A method is presented for calculating the design point efficiency potential of a multistage compressor. Design parameters that affect the efficiency are vector diagram shape, aerodynamic loading level, aspect ratio, solidity, clearances, airfoil maximum and edge thicknesses, annulus area contraction, Mach number, Reynolds number, airfoil surface finish, and part-span shroud placement. Losses associated with off-design operation, blading unsuited to the aerodynamic environment, or poor hardware quality are not considered. The loss model is constructed using rational fluid-dynamic elements, such as boundary layer theory, whenever feasible in an attempt to minimize empirical influences, although some empiricism inevitably enters. The resulting formulation is found to be in satisfactory agreement with multistage compressor experience that covers a wide range of the design parameters.

Introduction

When selecting an axial-flow compressor configuration for a specific application, there are usually several design features that are of importance. The list of important features always includes performance, initial cost, and maintenance cost, and often includes such features as weight, volume, and resistance to inlet flow distortions. In all cases the compressor must be surge-free and free of significant aerodynamically excited vibrations throughout its domain of operation.

When a new compressor design is contemplated, it is customary to conduct preliminary design studies aimed at providing quantitative assessments of these several features. At this point in the design process it is not necessary to specify detailed blade shapes, but rather it is desired to quantify factors that relate to cost, weight and volume, and to identify the *efficiency potential* of each design being studied. The term efficiency potential means the efficiency that can be expected if the detailed design (i.e., the specification of airfoil shapes, to be done later) is carried out using the best state-of-the-art design practices. Thus, the model described here does not attempt to deal with losses due to off-design operation, caused, for example, by mismatching between stages at part-speed operation, or to an improper selection of airfoil shapes for the aerodynamic environment such as would lead to blade rows operating in a choked condition. Nor is any attempt made to estimate the performance penalties due to poor blade quality, instrumentation in the air stream, inlet ducting, or discharge diffusers. The

purpose of the present paper is to provide a means for estimating the efficiency potential of candidate compressor designs.

Approach Employed in Establishing the Model

It should be stated at the outset that the authors are well aware that the real flow process in a multistage compressor is exceedingly complex, and that the loss model elements to be proposed are oversimplified. The approach to be taken can best be described as having an intermediate level of sophistication. The attempt is made to treat each loss source rationally, calling on fluid dynamic disciplines such as compressible boundary layer theory when it seems appropriate to do so, but inevitably some simplifying assumptions are made, such as that transition phenomena can be ignored, and that end-wall losses do not depend on Reynolds number and Mach number. Assumptions such as these are made when they seem to be appropriate, with the notion that they can be revised later if they appear to be responsible for a failure of the complete model to agree with compressor test experience.

In devising the model, four primary sources of losses were identified: (1) blade profile losses due to surface diffusion and trailing edge thickness, (2) losses due to end-wall boundary layers and clearances, (3) shock losses, and (4) losses due to part-span shrouds.

In developing the model, attention was first directed toward the first two of these loss sources, and only low-speed compressor configurations were at first considered. The influence of solidity, aspect ratio, clearances, and vector diagram shape could then be modeled before extending the procedure to account for the additional factors found in high-speed compressors. The procedure was refined by suitably adjusting it until good agreement was obtained with the efficiencies measured in a series of over 40 General Electric low-speed multistage compressor test configurations in which blade geometry parameters had been systematically varied. The basic validity of the blade profile loss and end-wall loss models was

Contributed by the Gas Turbine Division and presented at the Winter Annual Meeting, Houston, Texas, November 30-December 5, 1975 of THE AMERICAN SOCIETY OF MECHANICAL ENGINEERS. Manuscript received at ASME Headquarters July 28, 1975. Paper No. 75-WA/GT-6.

established during this initial phase.

In anticipation of the extension of the model to higher Mach numbers, the profile loss model was formulated using compressible boundary layer theory. In this way, a rational extension of the low-speed experience into the subsonic compressible regime has been obtained. For transonic and supersonic Mach numbers, shock-related losses are added, and part-span shroud losses are added when appropriate.

Each of the four primary sources of loss is described in more detail in the following sections. The paper concludes with a comparison of the model's predicted efficiency values with test data from both low-speed and high-speed compressors.

Blade Profile Loss

Compressible boundary layer theory has been employed to provide the basis for the profile loss model. This approach was chosen as a rational means to extend the classical two-dimensional, low-speed correlation of Lieblein [1]¹ into the Mach number and Reynolds number regions that are of interest to compressor designers. It also provides a means to account for the effects of streamtube contraction (annulus area ratio) on blade boundary layer growth. The effects of blade surface curvature could also have been included, but they were neglected for simplicity.

The general approach employed is as follows. The normalized rooftop-type blade surface velocity distributions shown in Fig. 1 were adopted, and suction-surface and pressure-surface boundary layers were calculated over ranges of Mach number, Reynolds number, and streamtube contraction for the velocity diffusion ratios of 1.3, 1.5, and 1.7, using the Mellor-Herring method [2]. In order to avoid the uncertainties associated with transition predic-

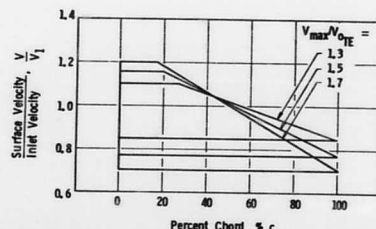


Fig. 1 Blade surface velocity distributions employed in the determination of the effects of Mach number and Reynolds number on blade profile loss using compressible boundary layer theory

tion, the boundary layers were assumed to be turbulent everywhere, although it is recognized that some laminar flow does almost certainly exist on well-designed multistage compressor airfoils. The adiabatic wall condition was also assumed. These calculations yielded trailing-edge momentum and displacement thickness values that were correlated with the independent variables, as will be described shortly.

It is of interest to note at this point that normalized velocity distributions were used for this study rather than normalized blade surface Mach number distributions. Both approaches were actually considered. However, the normalized Mach number approach was abandoned when it was calculated that the limiting Mach number ratio (i.e., the maximum suction-surface Mach number divided by the Mach number at separation), was Mach number dependent whereas the limiting velocity ratio was less so. For example, for uncontracted flow with a Reynolds number based on up-

¹ Numbers in brackets designate References at end of paper.

Nomenclature

A_a = annulus area	R = gas constant for air	θ = boundary layer momentum thickness
A_p^* = annulus area contraction ratio from cascade inlet to passage throat, equation (22)	Re = Reynolds number based on chord and blade row inlet relative velocity	ν = kinematic viscosity
A_s = part-span shroud ring area, equation (8)	Re_k = roughness Reynolds number based on equivalent sand-grain roughness and blade row inlet relative velocity	ξ = axial spacing between blade rows
b = tangential blade spacing	r = radius	ρ = static density
C_D = drag coefficient	r = average of blade row inlet and exit radii	σ = blade solidity, c/b
C_f = skin friction coefficient	s = entropy	τ = effective cascade passage area blockage due to blade thickness
C_u = tangential velocity of air in absolute frame of reference	T = static temperature	v = end-wall boundary layer tangential force thickness
c = chord length of compressor blade	t = thickness of blade or of part-span shroud	ω = loss coefficient, $\Delta P/(P - p)_1$
c_s = part-span shroud axial chord length	V = velocity of air relative to either rotors or stators	
D_{eq}^* = equivalent suction surface diffusion ratio, equation (16)	V_0 = free-stream velocity before wake mixing	
F_D = drag force	w = flow rate	
g = blade staggered spacing	β = air angle measured from axial direction	
H = boundary layer form factor	β = average of blade row inlet and exit air angles	
h = blade height	Γ = blade circulation	
h_1/h_2 = streamtube height ratio	Γ^* = blade circulation parameter, equations (18) and (19)	
K = empirical constant	γ = ratio of specific heats	
k = surface roughness dimension	Δ = denotes change in parameter	
k = mean surface roughness height	δ^* = boundary layer displacement thickness	
k_s = equivalent sand-grain roughness	ϵ = blade end clearance	
M = Mach number	η = efficiency	
N_B = number of blades	$\bar{\eta}$ = free stream efficiency without end-wall losses	
P = total pressure		
P_M = Mach number parameter, equation (13)		
$(\Delta p_R + \Delta p_{ST})$ = stage static-pressure rise		
$(q_{1R} + q_{1ST})$ = stage effective inlet dynamic head		

stream conditions and rooftop length of 200,000, the ratio of rooftop (i.e., maximum suction-surface) Mach number to separation Mach number varied from 1.79 to 2.08 as the inlet Mach number increased from 0.05 to 1.5, but the ratio of rooftop velocity to separation velocity varied only from 1.79 to 1.85 for the same range of Mach numbers. The normalized velocity distribution, therefore, has the advantage that the diffusion ratio for incipient separation is nearly independent of the Mach number level, which minimizes the interaction effects between the blade diffusion and Mach number independent variables.

When carrying out the boundary layer calculations for the rooftop velocity distributions, values of the suction-surface diffusion ratio ranged from 1.3 up to the value for which the boundary layer calculation procedure predicted turbulent separation, which depended somewhat on the other independent variables. The calculated sum of suction-surface and pressure-surface momentum thickness-to-chord ratios for incompressible flow with no streamwise contraction is shown in Fig. 2(a) as a function of diffusion ratio. The variation of form factor for the same conditions is shown in Fig. 2(b). The form factor is the ratio of the sum of the trailing-edge displacement thicknesses to the sum of the momentum thicknesses; when defined in this way it does not include any effect of blade trailing-edge thickness.

Fig. 2(a) also shows Lieblein's correlation of experimental data. These were obtained at a Reynolds number of 2.46×10^6 at a measuring plane somewhat downstream of the trailing edge where a representative value of the form factor was 1.08. In order to compare the calculated boundary layer characteristics with Lieblein's correlation, the calculated trailing-edge momentum thicknesses were converted to equivalent wake values for a wake in which the form factor was 1.08. To do this, the total loss for complete mixing was calculated from the trailing-edge boundary layer properties and the trailing-edge thickness/chord ratio of 0.003 that existed for the bulk of Lieblein's data, using a mixing loss analysis similar to that of Stewart [3]. The wake momentum thickness which would produce this same total loss, for an initial wake form factor of 1.08, was then calculated. This wake momentum thickness is also shown in Fig. 2(a). It can be seen that the wake momentum thickness is

greater than the trailing-edge momentum thickness by a significant amount for diffusion ratios above about 1.7, and closely parallels Lieblein's correlation in this range. This analytical result that momentum thickness increases just downstream of a cascade is due to the enlargement of the available flow area as the displacement thickness of the wake drops. The consequent reduction in free-stream velocity requires the momentum thickness to increase in order to represent a constant deficiency in momentum flux. This same result was also found in the analytical study of Lieblein and Roudebush [4]. The agreement between the trend of Lieblein's data and the calculated wake momentum thickness at high diffusion ratios is significant mainly as verification that the extrapolations of the calculated trailing-edge momentum thickness and form factor into the high diffusion ratio range shown in Figs. 2(a) and 2(b) were done sensibly.

At diffusion ratios below 1.7, the calculated wake and trailing-edge momentum thicknesses are virtually the same. These values are higher than Lieblein's data at these low diffusion ratios, and their trend is generally flatter in slope. The higher level is believed to be due to the considerable amount of laminar flow that existed in the cascades studied by Lieblein, whereas the calculated data presented here are for all-turbulent boundary layers. The steeper slope of Lieblein's data in the range of diffusion ratios from 1.35 to 1.7 is thought to be caused by a decrease in the amount of laminar flow on the blading with increasing aerodynamic loading.

The influence of compressibility on trailing-edge boundary layer characteristics was found to be twofold. First, there is the direct effect of Mach number, which causes a decrease in momentum thickness and an increase in form factor as inlet Mach number increases at constant diffusion ratio and Reynolds number. Second, a contraction of the streamtube is nearly always employed when there is noticeable density change across a blade row, and this affects the growth of the blade boundary layers.

The effect of inlet Mach number on trailing-edge momentum thickness and form factor is shown in Fig. 3. The curves show that the Mach number effect on momentum thickness is strongest at high diffusion ratios, while its effect on form factor is greatest at unity diffusion ratio. The calculated results giving the effect of Mach number on momentum thickness and form factor were essentially the same for all streamtube contraction ratios (inlet

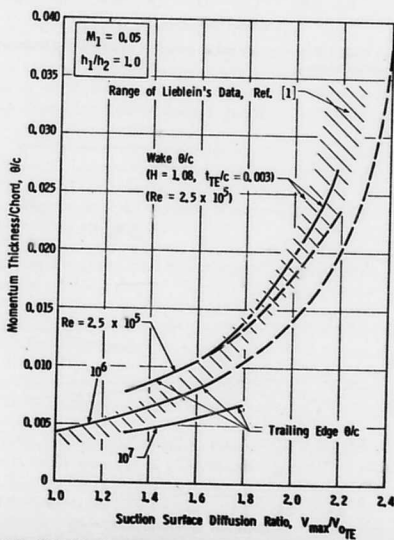


Fig. 2(a) Calculated trailing-edge and wake momentum thicknesses for two-dimensional, low-Mach-number flow over roof-top-type airfoils

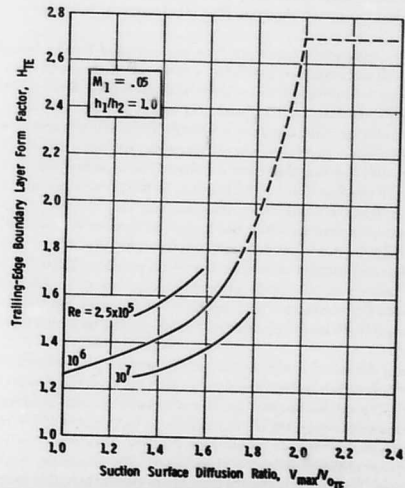


Fig. 2(b) Calculated trailing-edge boundary layer form factor for two-dimensional, low-Mach-number flow over roof-top-type airfoils

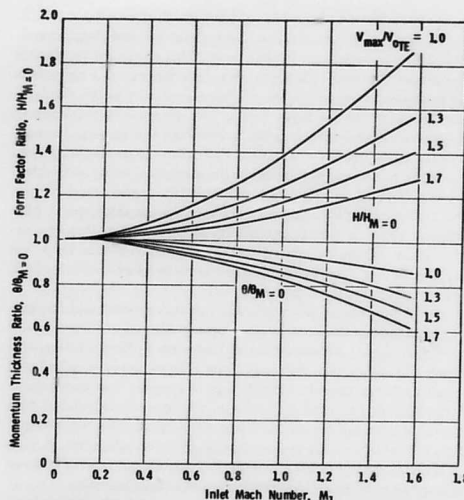


Fig. 3 Effect of inlet Mach number on calculated trailing-edge momentum thickness and form factor

streamtube height/exit streamtube height) from 0.6 to 1.7, and for all Reynolds numbers between 2.5×10^5 and 10^7 . The curves shown in Fig. 3 are composites of all the calculated data, but scatter of the calculated results with respect to these curves was less than ± 5 percent.

Streamtube contraction produced a linear variation in momentum thickness that was independent of inlet Mach number, Reynolds number or diffusion ratio, Fig. 4(a). The form factor was also affected linearly by streamtube contraction, as shown in Fig. 4(b), but in this case the effect was most severe at higher diffusion ratios. The contraction effects on momentum thickness and form factor calculated for all Mach numbers and Reynolds numbers collapsed to the curves shown in Figs. 4(a) and 4(b) to within ± 5 percent.

Since completely turbulent flow was assumed for the boundary layer calculations, they predicted a moderate decrease in both momentum thickness and form factor with increasing Reynolds number. The momentum thickness was found to vary as the -0.166 power of Reynolds number, while the form factor varied as the -0.060 power over the range of Reynolds numbers considered, 2.5×10^5 – 10^7 . For low Reynolds numbers it is expected that laminar flow will predominate on the blading. In the present model it is assumed that the momentum thickness will vary as the -0.5 power of Reynolds number when the Reynolds number is less than 2×10^5 . No transition effects are assumed for the form factor, and it is allowed to continue to vary as the -0.06 power at Reynolds numbers below 2×10^5 . These assumptions for low Reynolds number flow are quite arbitrary and certainly not rigorous, but their effect on overall efficiency appears reasonable, as will be shown in a later section.

As is discussed in more detail in Appendix 2, the critical roughness Reynolds number (based on equivalent sand roughness) is set at 90. The simple assumption is made that Reynolds number only influences the momentum thickness and form factor if the roughness Reynolds number is less than 90; above this value the boundary layer characteristics do not change with increasing Reynolds number. The result is that at high blade chord Reynolds numbers, the boundary layer characteristics (and thus the cascade profile losses) depend only on the ratio of blade surface roughness to

chord length and not at all on Reynolds number. Fig. 5 shows the variation of momentum thickness used in the blade profile loss model as a function of chord Reynolds number and surface roughness-to-chord ratio.

The efficiency prediction model uses these results to predict blade profile losses in the following manner:

1 The suction surface diffusion ratio, $V_{\text{max}}/V_{\text{OTE}}$ is calculated from the cascade geometry and the vector diagrams, accounting for blade thickness, annulus contraction and compressibility effects, as described in Appendix 1.

2 The ratio of trailing-edge momentum thickness to chord length and the trailing-edge form factor are found from Figs. 2(a) and 2(b), for a nominal value of Reynolds number of 1.0×10^6 , hydraulically smooth blades, a streamtube height ratio h_1/h_2 of 1.0, and a Mach number of 0.05. The momentum-thickness-to-chord ratio is increased by 0.0025 at all diffusion ratios, an empirical adjustment found to be necessary in order to match experimental data as described later.

3 A correction for inlet Mach number other than 0.05 is applied to the momentum thickness and form factor according to the curves given in Fig. 3.

4 Momentum thickness and form factor are corrected to streamtube convergence values other than 1.0 according to the curves given in Figs. 4(a) and 4(b).

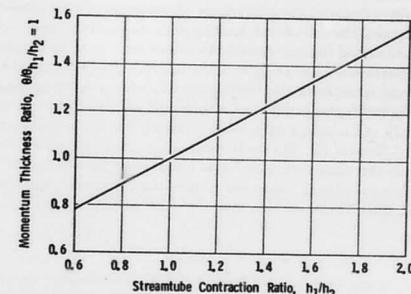


Fig. 4(a) Effect of streamtube height variation on calculated trailing-edge momentum thickness

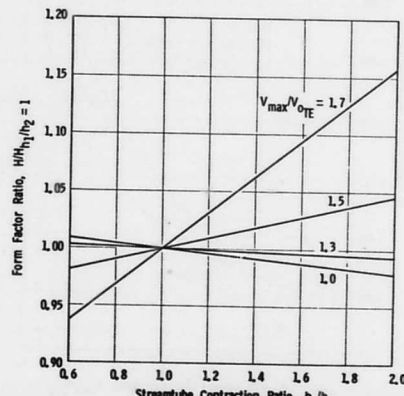


Fig. 4(b) Effect of streamtube height variation on calculated trailing-edge form factor

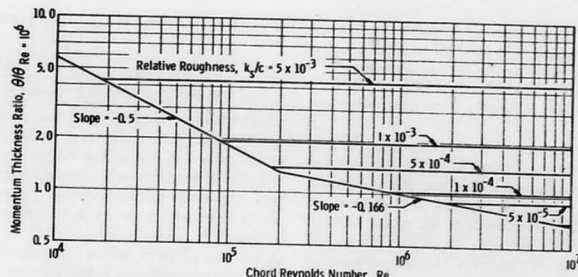


Fig. 5 Effect of Reynolds number and surface finish on calculated trailing-edge momentum thickness

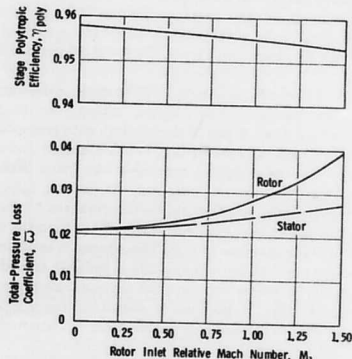


Fig. 6 Illustration of results from profile loss model

5 Reynolds numbers other than 1.0×10^6 and blade surface roughness require a final correction to momentum thickness according to Fig. 5. A similar correction factor is applied to form factor, but a -0.06 power variation is employed for all hydraulically smooth Reynolds numbers. Surface roughness is determined from equation (33) in Appendix 2.

6 The final values of momentum-thickness-to-chord and of form factor, including all correction factors, determine a new trailing-edge free-stream velocity, which in turn affects the magnitude of the diffusion ratio. An iteration is performed until all trailing-edge parameters converge.

7 The loss in total pressure relative to the blade row is determined from a constant-streamtube-height compressible-flow mixing process similar to that of Stewart [3] which accounts both for boundary layer thicknesses and blade trailing-edge thickness.

To give an illustration of results obtained from the profile loss model, it has been applied to a compressor stage consisting of a rotor cascade that receives swirl-free absolute flow and a stator cascade that removes all swirl. Each cascade has a solidity of 1.35, a maximum thickness-to-chord ratio of 0.06, and a trailing-edge thickness-to-chord ratio of 0.01. The ratio of axial velocity to blade speed is 0.6, and the axial velocity is maintained constant throughout the stage by means of streamtube convergence. The rotor diffusion factor is held constant at 0.45, and rotor Reynolds number is held constant at 1.0×10^6 .

The results are shown in Fig. 6. It is seen that the rotor loss coefficient nearly doubles as inlet Mach number increases from 0.1 to 1.5. The stator loss coefficient increases by about one-third. This

smaller increase for the stator is due mainly to the fact that the stator Mach number is lower (0.9 when the rotor Mach number is 1.5), but also due partly to an increase in stator Reynolds number and a slight reduction in diffusion ratio as rotor inlet Mach number increases. Despite the substantial increase in loss coefficients, however, the stage polytropic efficiency remains virtually constant. Essentially identical results were also obtained for stages with axial-velocity-to-blade-speed ratios of 0.4 and 0.8; the efficiency remained nearly constant despite large increases in the loss coefficients. This is a consequence of the definition of the conventional total-pressure loss coefficient. A loss coefficient defined in terms of energy quantities would, perhaps, be preferable. This has previously been pointed out by Stewart [3] and Brown [5].

Shock Losses

Formation of shocks on the blading at high subsonic and supersonic Mach numbers arises from both leading-edge bluntness effects and from the passage shock structure. The losses produced by both types of shocks are considered separately in the efficiency prediction model.

Leading-edge bluntness losses at supersonic upstream Mach numbers have been studied by Dr. D. C. Prince of General Electric, who developed the following expression for the entropy rise in a blade row due to bluntness:

$$\frac{\Delta s}{R} = -\ln \{1 - t_{LE}/(b \cos \beta_1) \times [1.28(M_1 - 1) + 0.96(M_1 - 1)^2]\} \quad (1)$$

This expression represents the trend of results from a method-of-characteristics-type analysis of the leading-edge flow field. It includes the loss due to local strengthening of the leading-edge shock that is contained within the passage as well as from the shock structure which propagates upstream of the leading-edge plane.

The leading-edge bluntness loss model is believed to be in good agreement with that presented recently by York and Woodard [6], and also has been checked against the experimental results of Goldberg [7] and of Reid and Uraszek [8]. For both of the experimental configurations, equation (1) predicts about two-thirds of the measured efficiency loss. This is considered to be reasonable agreement, since factors such as the substantial reduction in solidity produced when the edge was blunted in [8] could also have contributed to the loss in efficiency.

The passage shock loss model represents the shock-related losses associated with the diffusion process. The assumption is made that this loss is equivalent to the entropy rise of one oblique shock that reduces a representative passage inlet Mach number to unity Mach number. This applies so long as the exit Mach number is subsonic or sonic. When the exit Mach number is supersonic, the oblique shock is assumed to reduce the representative passage inlet Mach number to the exit Mach number. The representative passage inlet Mach number is a weighted average of the maximum

suction surface Mach number, deduced from equations (31) and (32), and the inlet Mach number. The selected weighting factor, chosen to give reasonable agreement with limited high-speed single-stage experience, weights the Mach number deduced from equations (31) and (32) six times as heavily as the upstream Mach number.

The authors are aware that it may be possible to design blading having lower shock losses than given by this model through the employment of prediffusion or multiple oblique shocks. Also, it may be possible to design to achieve lower maximum suction surface Mach numbers than those deduced from equations (31) and (32). On the other hand, other considerations, such as mechanical constraints on blade thickness and the need to minimize internal passage contraction to permit supersonic starting, may prevent the attainment of losses that are as low as those calculated.

Some results obtained from the shock loss model are given in Fig. 7. The ordinate is the total shock loss coefficient, including both leading-edge bluntness and passage shock losses. There are three symbols plotted for each case listed in the legend; these correspond to the rotor tip, mean-diameter, and hub streamlines. The legend also gives the stage efficiency obtained from test and the stage efficiency calculated from the complete loss model of this paper (including profile loss, end-wall loss, and part-span shroud loss), applied as described in a later section. In general, the model yields efficiencies that are somewhat higher than test data, except for the stage of [12]. In that case the calculated tip shock losses are lower than the trend of the data because of the supersonic exit Mach numbers employed, but still not low enough to match test experience. Further shock loss model refinements are obviously needed, but they are beyond the scope of the present paper.

End-Wall Loss

End-wall losses are included in the present model in a manner similar to that presented in 1969 [14]. The approach taken is based on an analysis that relates the efficiency loss due to the presence of end-wall effects to two properties of an end-wall boundary layer: its displacement thickness, δ^* , and its tangential-force thickness, v . The displacement thickness is a measure of the amount that the mass flow is reduced by the presence of the end-wall boundary layer from what it would be if the free-stream flow profiles were extended to the wall, and, likewise, the tangential-force thickness represents the amount that the tangential component of blade force is reduced from its free-stream value by the presence of the boundary layer. For incompressible flow in high-radius-ratio mul-

tistage compressors made up of repeating stages, it was shown [14] that

$$\eta = \tilde{\eta} \frac{1 - (\delta_h^* + \delta_t^*)/h}{1 - (v_h + v_t)/h} \quad (2)$$

where η is the stage efficiency, $\tilde{\eta}$ is the free-stream efficiency (i.e., the efficiency that would exist if there were no end-wall losses), and h is the annulus height. Values of δ^* and v deduced from detailed measurements of the flow profiles in several low-speed multistage research compressors were presented for both the hub and casing boundary layers behind both rotors and stators. The displacement thicknesses were normalized by the staggered spacing, g , between adjacent airfoils and related to the tip clearance level and stage pressure rise. Fairly tight correlations were obtained for the displacement thicknesses, but considerable data scatter was apparent in the tangential-force thickness correlations. Nonetheless, by assuming that v was a fixed fraction of δ^* , and by using a representative profile loss formulation, it turned out to be possible to construct fairly accurate pressure-rise and efficiency characteristic curves for a series of stages with aspect ratios varying from 2 to 5 and with tip clearances varying from 0.8–3.6 percent annulus height.

For present purposes, no attempt will be made to distinguish between hub and casing boundary layers; instead, their thicknesses will be added together. A plot of the research data prepared in this way, with rotor-exit and stator-exit values averaged and normalized by the average staggered spacing at the mean diameter, is shown in Fig. 8. For present purposes, the abscissa selected employs a stage pressure rise that has been normalized by the sum of the rotor and stator inlet dynamic heads rather than the dynamic head of the blade speed as in [14]. This change is contrary to the logic presented in [14], but it was made in order to spread out the data near stall for stages that have flat tops on their pressure-flow characteristics. Also, it provides a somewhat more meaningful measure of the stall margin available from a chosen operating point to stall.

The tip clearance values tabulated in Fig. 8 were obtained as follows: Since the research compressor blades were constructed with shanks, small clearances existed at their root ends ahead of and behind the shanks, and these clearance areas were divided by the full root chord to obtain a root-end clearance for each blade row. The root-end clearance was then added to the free-end tip clearance of the same blade row, and the sum was normalized by the staggered spacing at the mean diameter. The rotor and stator normalized

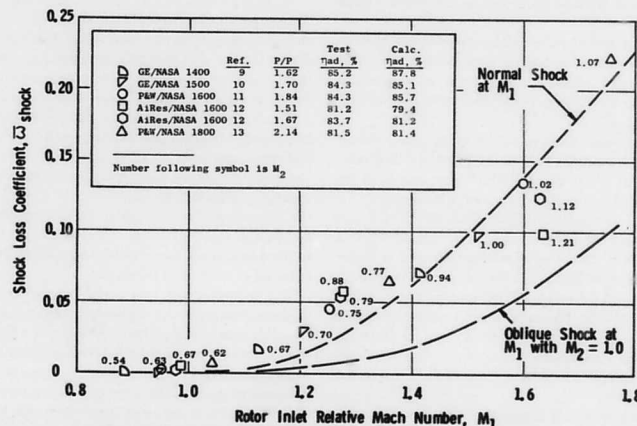


Fig. 7 Shock loss coefficients calculated for several high-speed fan stages

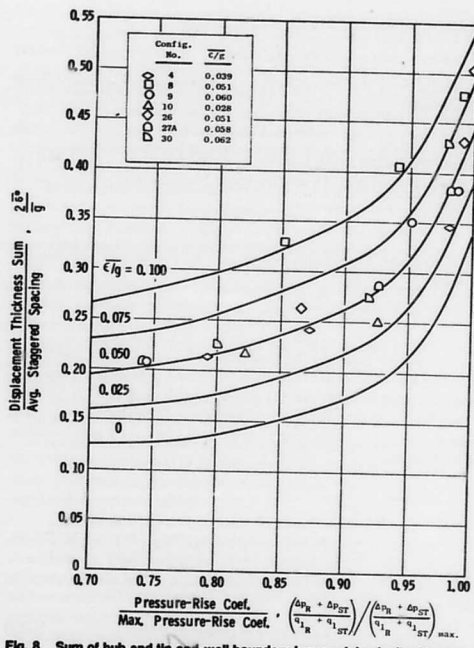


Fig. 8 Sum of hub and tip end-wall boundary layer axial velocity displacement thicknesses

clearances obtained in this manner were then averaged, using inlet dynamic heads for weighting, to obtain the stage-average normalized clearance, $\bar{\epsilon}/g$. The lines shown in Fig. 8 are related by

$$\frac{2\delta^*}{g} = \frac{2\delta^*}{g} \Big|_{\bar{\epsilon}/g=0} + 2\epsilon \left[\frac{\Delta p_R + \Delta p_{ST}}{q_{1R} + q_{1ST}} \right] / \left(\frac{\Delta p_R + \Delta p_{ST}}{q_{1R} + q_{1ST}} \right)_{\max} \quad (3)$$

It was observed in [14] that the axial gap between adjacent blade rows influences efficiency and peak pressure rise. Test data were presented showing that a compressor with very small axial gaps (8.3 percent of blade spacing in the tangential direction) had 1.1 points higher efficiency and 6 percent higher peak pressure rise than did the same compressor with the axial gaps opened to 43 percent of the tangential spacing. For present purposes, it will be assumed that these effects on performance occur because the axial gap influences the wall boundary layer thicknesses. This assumption is not entirely arbitrary because it is believed that the close proximity of a downstream blade row, moving relative to the upstream blade row, will tend to reduce the static pressure in local regions where the axial velocity is low, such as in the thick blade wakes that exist in the end-wall boundary layer. The static pressure reduction tends to increase the velocity for the same total pressure, but also tends to increase the total pressure by reducing the loss, thus enhancing the velocity increase and thinning the boundary layer. It is also quite possible that the flow unsteadiness associated with small axial gaps helps to delay wake growth.

The wall boundary layer measurements displayed in Fig. 8 were obtained from configurations having axial gap/tangential spacing ratios in the range from 0.3 to 0.4, and the curves shown can therefore be considered to apply in that range. Fig. 9 provides a means for adjusting the displacement thickness for axial gap effects when the axial gap is less than 70 percent of the tangential blade spacing. The general shape of the curve comes from engineering judg-



Fig. 9 Effect of axial gap between blade row edges on end-wall boundary layer displacement thickness

ment based on the authors' hypothesis of the phenomena involved, and the magnitude of the departure from unity was chosen to force agreement of the present efficiency model with the test data cited in the foregoing. It should be emphasized that the present model is not valid for large axial gaps, i.e., axial gaps larger than the 70 percent tangential spacing that represents the upper limit of the basic test data. With large axial gaps, other phenomena that are not included in the present approach play a role. It is obvious that annulus wall skin friction drag should then be included. Less obvious, but probably more important, is the fact that when annulus boundary layers build up on a stationary surface ahead of a stator, or a rotating surface ahead of a rotor, their skewness character changes and they are less able to sustain pressure rise in the blade row. Another frequent consequence of large axial spacing is the occurrence of significant annulus wall slope changes at the blade edges. Treatment of these phenomena is beyond the scope of the present paper.

The tangential-force thickness data obtained from the research compressor measurements are shown in Fig. 10. No consistent trend in the data is apparent, and the single line shown has been adopted.

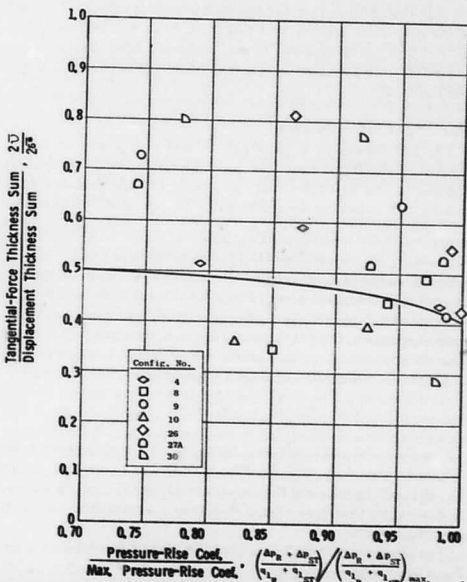


Fig. 10 Sum of hub and tip end-wall boundary layer tangential-force thicknesses

The present model consists of the lines shown in Figs. 8, 9, and 10, and the following equation, which is a restatement of equation (2):

$$\eta = \bar{\eta} \frac{1 - (2 \bar{\delta}^*/g) (\bar{g}/\bar{h})}{1 - (2 \bar{v}/2 \bar{\delta}^*) (2 \bar{\delta}^*/g) (\bar{g}/\bar{h})} \quad (4)$$

where (\bar{g}/\bar{h}) is the weighted average rotor and stator mean-diameter staggered spacing/annulus height ratio, the weighting function being the blade row inlet dynamic head.

It is realized that the present model is based on assumptions and data that are of limited scope and therefore of questionable generality. The applicability of the method to low aspect ratio compressors is of particular concern because, in such cases, the hub and casing boundary layers may overlap at the mean diameter. The research compressor boundary layer measurements were obtained from blading having aspect ratios of either 2.0 or 2.8, and with the solidities and staggers employed, there was almost always some free stream present between boundary layers, even close to stall. It was therefore possible to measure the full thicknesses of the boundary layers, and the ratio of full thickness to displacement thickness was found to vary between about 5 and 10, with 6 being a representative value. Taking this, and taking 0.25 as a representative value for $2\delta^*/g$, we conclude that the boundary layers will meet when h/g is less than 0.25(6) = 1.5. For a solidity of 1.3 and a stagger of 35 deg, this occurs when the aspect ratio, h/c , is less than $1.5 \cos 35 \text{ deg}/1.3 = 0.95$. It therefore seems that the present model should be expected to work reasonably well with aspect ratios down to at least about unity, and the compressor data mentioned later indicate that it does. Furthermore, it seems likely that, even if the hub and casing boundary layers did intersect, the losses that they represent would not be reduced in any substantial way by their interference, and equation (4), with values supplied by Figs. 8, 9, and 10, is therefore employed in the present end-wall-loss model for all aspect ratios. However, for the purpose of calculating a free-stream axial velocity for use in the profile loss, shock loss, and part-span-shroud loss models, $2\delta^*/h$ is taken as 0.17 if the value of it deduced from Figs. 8 and 9 is greater than 0.17. The limit 0.17 was chosen because it corresponds to a parabolic axial velocity distribution that has the wall velocities equal to one-half of the maximum velocity, and this is about as nonuniform as the distribution can be expected to get. Obviously, additional data are needed to justify the present method when aspect ratios are much less than unity.

Part-Span Shroud Loss

The loss caused by a part-span shroud is represented in the present model by its drag. For incompressible flow in a straight cascade, it can be shown that the change in total pressure after mixing, ΔP , caused by the addition of a drag force, F_D , is given by

$$\frac{-\Delta P}{\rho} = \frac{F_D V_\infty}{w} \quad (5)$$

where w is the mass flow rate, V_∞ is the vector mean of the upstream and downstream velocities, and ρ is the fluid density. For compressible flow in a contracting cascade no such simple relationship is apparent, but the following approach seems to offer a reasonable approximation. In a straight duct, which is a special case of a cascade, one-dimensional gasdynamics yields, for small F_D ,

$$T_\infty \Delta s = \frac{F_D V_\infty}{w} \quad (6)$$

where T_∞ is the static temperature and Δs is the entropy increase caused by the addition of F_D . This has the same form as equation (5), so it will be assumed that equation (6), like (5), can be applied to blade rows that have a large change in V across them as well as to straight ducts.

The shroud drag coefficient based on shroud frontal area is defined as

$$C_{D_s} = \frac{F_D}{\frac{1}{2} \rho_\infty V_\infty^2 A_s \cos \beta_\infty} \quad (7)$$

where β_∞ is the vector mean flow angle and

$$A_s = 2\pi r_s t_s \quad (8)$$

r_s and t_s being the shroud radius and thickness, respectively. From continuity,

$$w = \rho_\infty V_\infty \cos \beta_\infty A_{a_\infty} \quad (9)$$

where A_{a_∞} is the mean annulus area. When equations (7) and (9) are substituted into (6), and the mean Mach number

$$M_\infty = \frac{V_\infty}{\sqrt{\gamma R T_\infty}} \quad (10)$$

is introduced, the entropy rise caused by the shroud addition becomes

$$\frac{\Delta s}{R} = C_{D_s} \frac{\gamma}{2} M_\infty^2 \frac{A_s}{A_{a_\infty}} \quad (11)$$

In order to estimate the magnitude of C_{D_s} , the drag coefficient correlations of Hoerner have been employed. The drag is presumed to come from two sources: (1) shroud profile drag and (2) interference drag generated at the intersections of the shroud wings and the airfoils. For profile drag Hoerner [15] gives, for a swept uncambered airfoil,

$$C_{D_s} (\text{profile}) = \frac{C_f}{\cos \beta_\infty} \times \left[2 \frac{c_s}{t_s} + 4 \cos \beta_\infty + 120 P^3 M \left(\frac{t_s}{c_s} \right)^3 \cos \beta_\infty \right] \quad (12)$$

where C_f is the skin friction coefficient, c_s is the shroud chord in the axial direction, and

$$P_M = (1 - M_\infty^2 \cos^2 \beta_\infty)^{-1/2} \quad (13)$$

Equation (12) applies to a swept airfoil. Elsewhere, Hoerner [16] indicates that, for an elliptical profile, which more closely resembles the shapes employed for part-span shrouds, the exponent on (t_s/c_s) in the last term in (12) should be 2 rather than 3.

For interference drag Hoerner [17] gives, in terms of the present drag coefficient definition,

$$C_{D_s} (\text{int.}) = \frac{2}{\cos \beta_\infty b} \times \left[0.75 \left(\frac{t_s}{c_s / \cos \beta_\infty} \right) - 0.0003 \left(\frac{c_s / \cos \beta_\infty}{t_s} \right)^2 \right] \quad (14)$$

where $b = 2\pi r_s N_B$ is the length of a shroud segment. In writing equation (14), it was assumed that shroud sweep does not affect interference drag.

The total shroud drag coefficient is taken as the sum of equations (12) and (14), but with the following adjustments. In equation (12), the exponent on (t_s/c_s) is taken as 2 rather than 3, and a representative skin friction coefficient of 0.006 is assumed. In equation (14) the last term is neglected because it is usually small, and the remainder is arbitrarily doubled in recognition of the fact that the airfoils that the shroud wings intersect have adverse pressure gradients, whereas the data on which (14) is based were obtained without a pressure gradient. The compressibility adjustment is also applied to equation (14). The final expression then is

$$C_{D_s} = K_s \left[0.012 \left[\frac{c_s / t_s}{\cos \beta_\infty} + 2 + 60 P^3 M \left(\frac{t_s}{c_s} \right)^2 \right] + 3 P^3 M \left(\frac{t_s}{b} \right) \left(\frac{t_s}{c_s} \right) \right] \quad (15)$$

where K_s is an empirical constant to be determined from experience.

In order to determine K_s , available test data from rotor blade rows were employed. The data were obtained from radial traverse probe measurements at rotor exit, and it appeared in the form of either an efficiency plot or a loss-coefficient plot. In either case, the plot was observed to have a bump near the shroud location re-

flecting the shroud loss, and it was necessary to estimate, from values adjacent to the bump, what the loss would have been if the shroud were not present. This is a somewhat uncertain process. In some cases, when there appeared to be two equally justifiable interpretations of what constituted the bump, two shroud-free loss fairings were done and both were used. In all cases, the shroud loss so determined was expressed in terms of an entropy rise chargeable to the shroud, and equation (11) was employed to determine the test drag coefficient.

The test drag coefficients are plotted in Fig. 11 versus the drag coefficients calculated from equation (15) with $K_s = 1.0$. Considerable scatter is apparent, which is not surprising because (1) the test data reduction method described is unavoidably crude, (2) the actual shrouds were not always aerodynamically equivalent to elliptical cylinders perfectly aligned with the flow, and (3) the shroud chordwise placement and the rotor blade passage shapes were not all equal.

Based on Fig. 11, K_s is taken as 1.8. The present model, then, consists of equation (11), with C_D , obtained from equation (15) with $K_s = 1.8$.

Comparisons With Compressor Test Data

A simplified computer program was written in order to predict the efficiency potential of multistage compressors and to compare these predicted efficiencies with the test data. The sequence of calculations is outlined below:

- Compressor geometry, inlet flow properties, speed, airflow, stage exit static pressures and swirl angles, and estimated stage efficiencies are input to the program, and pitchline vector diagrams are calculated. These vector diagrams satisfy the continuity and turbomachinery energy input equations on a pitchline basis. The annulus blockage effect of end-wall boundary layers is accounted for in this step using the model's end-wall boundary layer displacement thickness correlation. The ratio of pressure-rise coefficient to max pressure-rise coefficient, needed for each stage, is also input,

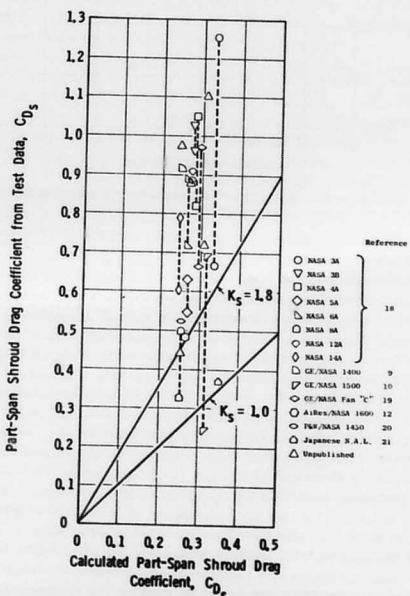


Fig. 11 Comparison of calculated part-span shroud drag coefficients, from equation (15) with $K_s = 1.0$, with experimental data

or is provided by a stall correlation, the description of which is beyond the scope of the present paper.

- In the present formulation, approximate tip and hub vector diagrams are calculated by assuming radially constant total pressure, total temperature and axial velocity at each station. At stator exit calculation stations the absolute air angle is assumed to be radially constant, while the turbomachinery energy equation is satisfied at rotor exit stations. The radial-equilibrium equation is not necessarily satisfied in this approximation.

- The entropy rise contributions of rotor and stator blade profile losses and shock losses are added together for the tip, pitch, and hub sections of each stage. These are then area-averaged radially and converted to an average free-stream efficiency for the stage. This efficiency is then modified to reflect the end-wall losses. Finally, the radially-averaged entropy rise due to part-span shrouds is added, and the total entropy rise is converted to a predicted stage efficiency.

- The predicted total-temperature rise of each stage is calculated, consistent with the input pressure rise and the predicted stage efficiency. The individual predicted stage work inputs are added and used with the known overall total-pressure ratio to find the predicted overall adiabatic efficiency.

The validity of the efficiency prediction model was first checked by comparing its calculated efficiencies with results from 41 configurations tested in the General Electric Low Speed Research Compressor facility described in [14]. These test configurations, each of which consists of three or four repeating stages, encompass ranges of aspect ratio from 1 to 5, pitchline solidity from 0.6 to 2.0, clearance from 0.8 to 3.7 percent of annulus height, stagger angle from 22 to 42 deg and reaction from 0.45 to 0.68. All blading was unshrouded, and the airfoils made use of modified NACA 65-Series thickness distributions on circular-arc meanlines. Since Mach number was less than 0.15 in all tests, only the blade profile loss and end-wall loss portions of the efficiency model were exercised, and the comparison with the test data was not complicated by the compressibility, shock loss and roughness factors found in high-speed compressors. Test Reynolds numbers ranged from 1.3 to 3.6×10^5 .

In the process of checking out the model with respect to the low-speed data, the need for an empirical adder to the momentum thickness given by the boundary layer calculations was identified and incorporated. The adder is relatively small; the momentum-thickness-to-chord ratio at a Reynolds number of 1.0×10^6 , Mach number of 0.05, and streamtube height ratio of 1.0, Fig. 2(a), is increased by 0.0025 at all values of diffusion ratio. This adjustment reduces the calculated efficiency by about 1.0 to 1.5 point below that given by the unadjusted boundary layer loss model. It was found to be required to use an empirical adder only on the profile losses and not on end-wall losses.

A comparison of test peak efficiencies with those calculated at the flow rate for which the peak was measured for the 41 low-speed configurations is given in Fig. 12. All but three data points were calculated to within 1.0 point, and 70 percent of the cases were calculated to within 0.5 point. For the three points for which the calculated efficiencies differ from the test data by more than 1.0 point, other evidence is available to suggest that the trend of the model is more reasonable than that of the data, and measurement inaccuracies are suspected. For example, the two data points in Fig. 12 having a stage-average aspect ratio of 2.1 actually employ the same rotor blades as the 2.0-aspect-ratio configurations and only differ by using higher aspect ratio stators. The design changes made do not appear to be sufficient to raise these two configurations nearly 2 points in efficiency above the trend of the other data. The other configuration not agreeing with the efficiency prediction model, the 2.8-aspect-ratio compressor with a test efficiency of 0.878, achieved an efficiency of 0.890 when the rotor blades were restaggered closed by 5.1 percent. The closed-stagger case would agree well with the model, and this observation casts some doubt on the measurement accuracy for the test configuration with the low efficiency.

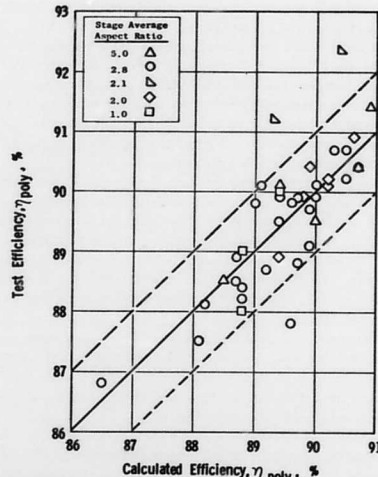


Fig. 12 Comparison of calculated polytropic efficiency of low-speed multistage compressors with experimental results

The good agreement achieved between the model and the low-speed test data established a reasonable level of confidence in the basic blade profile and end-wall loss models. This model gives a good estimate of the losses to be expected from well-designed airfoils of the type currently employed in most multistage compressors, when operated near minimum loss incidence at low speed. This level of agreement allowed the next step to be taken, that of comparing the results of the complete model to test data from a number of high-speed multistage compressors.

Since Reynolds number and surface finish effects, as well as compressibility effects, are significant elements in the loss model, considerable attention was paid to data from the NACA 8-stage compressor. In particular, it was important to obtain good agreement with the trends of the performance data from both the long-chord and medium-chord versions of this compressor showing the effects of Reynolds number variations. Fig. 13 compares the efficiency measured over a range of average chord Reynolds number at 100 percent design speed to that calculated by the model. The test data of [22] show a decrease in efficiency of 12 points for the medium-chord version as Reynolds number decreased from 600,000 to 50,000. The efficiency prediction model calculated just slightly less than a 10-point decrease in efficiency, which is considered good agreement, particularly since stage mismatching effects are not considered by the model. The data of [23] for the long-chord compressor show less variation with Reynolds number than for the medium-chord version. The model predicts a greater effect on efficiency than the data indicate in this case.

The calculated level of efficiency is greater than that demonstrated at 100 percent speed and high Reynolds numbers by about two points. Clearance levels were not reported, however, and for the present calculations were based on some unpublished data relating to an earlier version of the compressor (24); the later versions may well have had larger clearances than the first. These later versions also had a number of mechanical compromises, as noted in (25), which may well have hurt their efficiency but which are not modeled by the efficiency prediction technique.

The efficiency prediction model calculated that the efficiency of the version having long-chord stage 1 and stage 2 blading would be approximately 1 point poorer than the baseline version at the same average Reynolds number and clearance. The test data do indicate the long-chord version was somewhat lower in efficiency at high

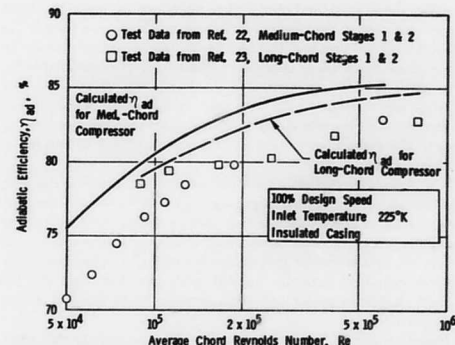


Fig. 13 Effect of Reynolds number on efficiency of NACA high-speed 8-stage compressors

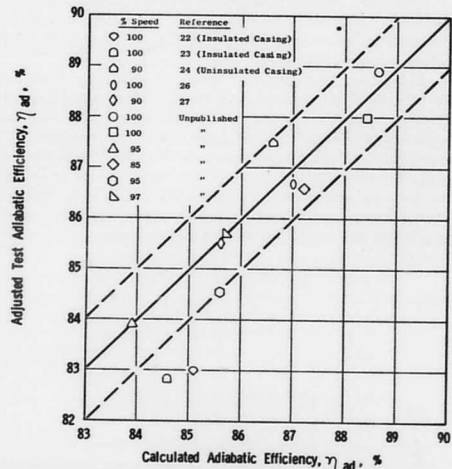


Fig. 14 Comparison of calculated and experimental adiabatic efficiency for high-speed multistage compressors

Reynolds numbers, but not by as much as was predicted. However, it is not known if the same clearances were held in both versions.

A final comparison with experimental data is presented in Fig. 14. Data points for a number of high-speed compressors having from 2 to 17 stages, design total-pressure ratios from 2.8 to 16.8, design corrected tip speeds from 330 m/s to 445 m/s, and average blading aspect ratios from 1.26 to 2.28 are included in this comparison. Individual rotor blade aspect ratios varied from 0.66 to 3.57. Running tip clearances for each machine were based on available estimates. Shrouded stators were treated as if they were cantilever with the tip clearance taken to be 20 percent larger than that of the preceding rotor. The experimental points were chosen as the peak efficiency for the particular speed at which the stages appeared to be best matched. This was done in an attempt to compare the data with the model's prediction only when losses due to off-design operation were likely to be small. When tests were conducted at more than one Reynolds number the comparison was made at the Reynolds number for which most of the development testing was done. In several cases the experimental data have been

adjusted upward from the actual test measurements in order to reflect estimated losses due to extensive use of strain gages or fixed aerodynamic probes in the test vehicle. The adjustment, when applied, was a minimum of 0.3 point and was a maximum of 0.9 point for very heavily instrumented smaller compressors. Nearly every configuration shown in Fig. 14 had inlet ducting containing struts or other structural parts. The losses from these are absorbed in the test efficiency but not in the predicted value. The predicted peak efficiency given by the model is nearly always somewhat higher than the experimental data, usually within 1.0 point.

The model is unable to predict an efficiency as high as reported for the original NACA 8-stage compressor, [24]. It is, however, able to predict an efficiency close to that reported in [27] for a 0.304 scaled version of the same machine. Also, the data from [24] were recorded at one-third atmospheric inlet pressure with 255 K inlet air temperature. Tests of a later configuration [22] showed that adding insulation to the compressor casing reduced the measured efficiency by about 0.8 point at these inlet conditions. The experimental data shown in Fig. 14 from [22, 23] are for the insulated casing tests. It is expected that if the configuration in [24] had been insulated, its efficiency would have been closer to that predicted by the model. In general, the authors consider these to be the desired results. Since the model does not consider all sources of loss, and is intended to give the peak efficiency potential of a given configuration when fully developed, the calculated efficiency values should be slightly higher than most experimental data.

Conclusions

A method has been provided for determination of the efficiency potential of a multistage axial-flow compressor. Four loss sources have been identified and quantified. These are:

1 *Profile Loss.* Compressible turbulent boundary layer theory has been employed to relate profile loss to suction surface diffusion ratio, streamtube contraction, Mach number, Reynolds number, and certain geometric blading parameters. It was found to be necessary to add a constant increment to the momentum thickness calculated from the boundary layer theory in order to match test experience. The increment size is equivalent to about 1.5 point in compressor efficiency. The reason that this increment is needed in unknown, but is probably related to flow unsteadiness.

Two noteworthy findings from the profile loss model are:

(a) At constant Reynolds number and Mach number, loss depends on streamtube contraction as well as on diffusion ratio. End-wall secondary flows that convect fluid onto the suction surface may increase free-stream loss by contracting the suction surface boundary layer.

(b) As Mach number is increased at constant Reynolds number and diffusion factor, and with streamtube contraction increased to maintain similar velocity triangles, the total-pressure loss coefficient increases significantly, but stage polytropic efficiencies remain virtually unchanged. This is a consequence of the definition of the conventional total-pressure loss coefficient.

2 *End-Wall Loss.* The mass flow deficit in an end-wall boundary layer, represented by its displacement thickness, causes an efficiency decrease, but this is partly offset by the deficit in tangential blade force in the boundary layer. Because of this offsetting factor, low aspect ratio compressors, with their relatively thick end-wall boundary layers, may not have substantially poorer efficiencies than those of higher aspect ratio compressors.

3 *Shock Loss.* The proposed passage shock model is obviously over-simplified but results based on it seem to be in reasonable agreement with limited experience. The contribution to shock losses caused by leading-edge thickness can be substantial at the higher Mach numbers.

4 *Part-Span Shroud Loss.* Rotor tests show that this loss is typically twice that which would be expected based on shroud profile drag and interference drag estimates.

Acknowledgments

The authors wish to thank the Aircraft Engine Group of General

Electric Company for its permission to publish this paper. The authors are also indebted to J. S. Keith for his recommendations and assistance in carrying out the compressible boundary layer calculations, D. C. Prince, Jr., for providing the leading-edge-thickness shock loss model, P. N. Szucs for his ideas concerning part-span shroud losses, and J. P. Scott for compiling the part-span shroud data.

References

- 1 Lieblein, S., "Loss and Stall Analysis of Compressor Cascades," *Journal of Basic Engineering*, TRANS. ASME, Sept. 1959, pp. 387-400.
- 2 Albers, J. A., and Gregg, J. L., "Computer Program for Calculating Laminar, Transitional and Turbulent Boundary Layers for a Compressible Axisymmetric Flow," NASA TN D-7521, April 1974.
- 3 Stewart, W. L., "Analysis of Two-Dimensional Compressible-Flow Loss Characteristics Downstream of Turbomachine Blade Rows in Terms of Basic Boundary-Layer Characteristics," NACA TN 3515, July 1955.
- 4 Lieblein, S., and Roudebush, W. H., "Low-Speed Wake Characteristics of Two-Dimensional Cascade and Isolated Airfoil Sections," NACA TN 3771, Oct. 1956.
- 5 Brown, L. E., "Axial Flow Compressor and Turbine Loss Coefficients: A Comparison of Several Parameters," ASME Paper No. 72-GT-18, presented at the Gas Turbine and Fluids Engineering Conference and Products Show, San Francisco, Calif., Mar. 1972.
- 6 York, R. E., and Woodward, H. S., "Supersonic Compressor Cascades—An Analysis of the Entrance Region Flow Field Containing Detached Shock Waves," ASME Paper No. 75-GT-33, presented at the Gas Turbine Conference, Houston, Texas, Mar. 1975.
- 7 Goldberg, T. J., "Experimental Investigation of an Axial-Flow Supersonic Compressor Having Sharp Leading-Edge Blades With an 8-Percent Mean Thickness-Chord Ratio," NACA RM L54K18, Feb. 1955.
- 8 Reid, L., and Urusek, D. C., "Experimental Evaluation of the Effects of a Blunt Leading Edge on the Performance of a Transonic Rotor," ASME Paper No. 73-GT-60, presented at the Gas Turbine Conference and Products Show, Washington, D. C., Apr. 1973.
- 9 Koch, C. C., Bilwakesh, K. R., and Doyle, V. L., "Evaluation of Range and Distortion Tolerance for High Mach Number Transonic Fan Stages—Task I Stage Final Report," NASA CR-72806, Aug. 1971.
- 10 Bilwakesh, K. R., "Evaluation of Range and Distortion Tolerance for High Mach Number Transonic Fan Stages—Task II Stage Data and Performance Report for Undistorted Inlet Flow Testing," NASA CR-72787, Jan. 1971.
- 11 Sulam, D. H., Keenan, M. J., and Flynn, T. J., "Single-Stage Evaluation of Highly-Loaded High-Mach Number Compressor Stages II—Data and Performance, Multiple-Circular-Arc Rotor," NASA CR-72694.
- 12 Ware, T. C., Kobayashi, R. J., and Jackson, R. J., "High-Tip-Speed, Low-Loading Transonic Fan Stage Part 3—Final Report," NASA CR-121263, Dec. 1974.
- 13 Morris, A. L., and Sulam, D. H., "High-Loading, 1800 ft/sec Tip Speed Transonic Compressor Fan Stage II—Final Report," NASA CR-120991, Dec. 1972.
- 14 Smith, L. H., Jr., "Casing Boundary Layers in Multistage Axial-Flow Compressors," *Flow Research on Blading*, L. S. Dzurin, ed., Elsevier Publishing, Amsterdam, Netherlands, 1970.
- 15 Hoerner, S. F., *Fluid-Dynamic Drag*, published by the author, Midland Park, N. J., 1965, pp. 15-21.
- 16 Ibid., pp. 3-11.
- 17 Ibid., pp. 8-10.
- 18 Edgar, G. M., and Sandercock, D. M., "Some Observed Effects of Part-Span Dampers on Rotating Blade Row Performance Near Design Point," NASA TM X-2696, Jan. 1973.
- 19 Giffin, R. G., Parker, D. E., and Dunbar, L. W., "Experimental Quiet Engine Program—Aerodynamic Performance of Fan C," NASA CR-120981, Aug. 1972.
- 20 Messenger, H. E., and Kennan, M. J., "Two-Stage Fan II—Data and Performance With Redesigned Second Stage Rotor Uniform and Distorted Inlet Flows," NASA CR-134710, Oct. 1974.
- 21 Fujii, S., "Some Studies of Front Fans With and Without Snubbers," ASME Paper No. 72-GT-4, presented at the Gas Turbine and Fluids Engineering Conference and Product Show, San Francisco, Calif., Mar. 1972.
- 22 Geye, R. P., and Lucas, J. G., "Investigation of Effects of Reynolds Number on Over-All Performance of an Eight-Stage Axial-Flow Compressor With Two Transonic Inlet Stages," NACA RM E56L11a, Feb. 1957.
- 23 Sievers, G. K., Geye, R. P., and Lucas, J. G., "Investigation of Reynolds Number Effects on Performance of an Eight-Stage Axial-Flow Research Compressor With Long- and Medium-Chord Lengths in the Two Transonic Inlet Stages," NACA RM E57J30, Feb. 1958.
- 24 Geye, R. P., Budinger, R. E., and Voit, C. H., "Investigation of a High-Pressure-Ratio Eight-Stage Axial-Flow Research Compressor With Two Transonic Inlet Stages II—Preliminary Analysis of Overall Performance," NACA RM E55J06, Dec. 1953.
- 25 Geye, R. P., and Voit, C. H., "Investigation of a High-Pressure-Ratio Eight-Stage Axial-Flow Research Compressor With Two Transonic Inlet Stages IV—Modification of Aerodynamic Design and Prediction of Performance," NACA RM E55B28, June 1955.

26 Wiggins, J. O., and Waltz, G. L., "Some Experience in the Scaling of the NASA 8-Stage Transonic Axial Flow Compressor," SAE Paper 720711 presented at the National Combined Farm, Construction and Industrial Machinery and Powerplant Meetings, Milwaukee, Wis., Sept. 1972.

27 Ruggeri, R. S., and Benser, W. A., "Performance of a Highly Loaded Two-Stage Axial Flow Fan," NASA TM X-3076, 1974.

28 Anon., "Surface Texture," ASA B46.1—1962, ASME American Standard.

29 Nikuradse, J., "Laws of Flow in Rough Pipes," National Advisory Committee for Aeronautics, Technical Memorandum 1292, Nov. 1950 (translation).

30 Speidel, L., "The Effect of Surface Roughness on the Flow Losses in Plane Blading Grids," translation from *Forschung auf dem Gebiete des Ingenieurwesens*, Vol. 20, No. 5, 1954, pp. 129–140.

31 Nece, R. E., and Daily, J. W., "Roughness Effects on Frictional Resistance of Enclosed Rotating Disks," *Journal of Basic Engineering*, TRANS. ASME, Sept. 1960, pp. 553–560.

32 Young, A. D., "The Drag Effects of Roughness at High Subcritical Speeds," *Journal of Royal Aeronautical Society*, Vol. 54, 1950, pp. 534–540.

33 Schlichting, H., *Boundary Layer Theory*, McGraw-Hill, New York, Fourth ed., 1960, p. 558.

34 Bammert, K., and Milsch, R., "Boundary Layers on Rough Compressor Blades," ASME Paper No. 72-GT-48, presented at the Gas Turbine & Fluid Engineering Conference and Products Show, San Francisco, Calif., Mar. 1972.

35 Lindsey, W. H., "The Development of the Armstrong Siddeley Mamba Engine," *Journal Royal Society*, Vol. 53, 1949, pp. 137–173.

36 Turner, R. C., and Hughes, H. P., "Tests on Rough Surfaced Compressor Blading," NGTE C.P. No. 306 (17,933) A.R.C. Technical Report, 1956.

37 Moses, J. J., and Serovy, G. K., "Effect of Blade-Surface Finish on Performance of a Single-Stage Axial-Flow Compressor," NACA RM E51C09, Apr. 1951.

38 Nixon, R. A., and Cairney, W. D., "Scale Effects in Centrifugal Cooling Water Pumps for Thermal Power Stations," National Engineering Laboratory, Glasgow, NEL Report No. 505, Apr. 1972.

39 Schlichting, H., *Boundary-Layer Theory*, Handbook of Fluid Dynamics, V. L. Streeter, ed., Section 9, 1961, pp. 9–64.

APPENDIX 1

Derivation of Generalized Blade Diffusion Ratio

In reference [1] Lieblein developed an Equivalent Diffusion Ratio, D_{eq}^* , which is a semiempirical formulation for the ratio of maximum suction surface velocity to trailing edge velocity, applicable for two-dimensional cascades of 10 percent-thick airfoils operating in incompressible flow. It is the purpose of this appendix to provide an alternative semiempirical expression that is somewhat more general. In particular, it desired to remove the thickness restriction, to include an approximate adjustment for compressibility and streamtube contraction effects, and to formulate the expression in such a way that it applies (approximately) to both rotating and stationary blade rows that may have a mild radius change. Only operation at minimum-loss incidence will be considered.

The approach taken in formulating the more general expression for D_{eq}^* was to equate this parameter to the product of three velocity ratios that were then examined separately:

$$D_{eq}^* = \frac{V_{max}}{V_{0TE}} = \frac{V_p}{V_1} \times \frac{V_{max}}{V_p} \times \frac{V_1}{V_{0TE}} \quad (16)$$

where V_p is the mean passage velocity in the throat region where the suction surface velocity is greatest.

The ratio of passage velocity to upstream velocity, V_p/V_1 , was treated as described below. V_p is composed of a tangential component that is affected by circulation, and an axial component that is affected by blade thickness blockage, streamtube contraction, and compressibility. Fig. 15 illustrates these concepts and the nomenclature used.

It was assumed that the change in tangential velocity from upstream to the passage region is proportional to blade circulation, and thus

$$V_{up} = V_{u1} - K_1 \Gamma / b = V_1 \sin \beta_1 - K_1 V_1 \sigma \Gamma^* \quad (17)$$

where $\Gamma^* = \Gamma/c V_1$ is a circulation parameter, and K_1 is an empirical constant to be determined later. For the general case,

$$\Gamma^* = (r_1 C_{u1} - r_2 C_{u2}) / \sigma V_1 \quad (18)$$

and for a two-dimensional incompressible cascade

$$\Gamma^* = \cos \beta_1 (\tan \beta_1 - \tan \beta_2) / \sigma \quad (19)$$

A continuity equation for the region near the cascade throat was written as:

$$\rho_p V_{zp} \left(1 - \frac{\tau}{b} \right) A_{ap} = \rho_1 V_1 \cos \beta_1 A_{a1} \quad (20)$$

For the streamtube contraction term it was assumed that the cascade throat occurred at one-third the axial length of the cascade:

$$A_{ap} = A_{a1} - \frac{1}{3} (A_{a1} - A_{a2}) \quad (21)$$

Thus, the axial velocity in the cascade throat region is:

$$V_{zp} = V_1 \cos \beta_1 / \left(\frac{\rho_p}{\rho_1} A_{p*} \right) \quad (22)$$

where

$$A_{p*} = \left(1 - \frac{\tau}{b} \right) \left(1 - \frac{A_{a1} - A_{a2}}{3 A_{a1}} \right)$$

The thickness-blockage term in A_{p*} was represented by:

$$\left(1 - \frac{\tau}{b} \right) = 1 - K_2 \sigma \left(\frac{t_{max}}{c} \right) / \cos \beta \quad (23)$$

where K_2 was an empirical constant to be determined later, and β was the average air angle in the cascade.

The effect of compressibility enters through the density ratio in equation (22). This was approximated as:

$$\frac{\rho_p}{\rho_1} = 1 + \frac{d\rho}{\rho} \quad (24)$$

One-dimensional isentropic gas dynamics relationships for a simple area change process allow the foregoing to be expressed as:

$$1 + \frac{d\rho}{\rho} = 1 - M^2 \frac{dV}{V} = 1 - M_z^2 \frac{dV_z}{V_z} - \frac{M_z^2 dV_u^2}{2 V_z^2} \quad (25)$$

The assumption implied by using the differential form is that the compressibility effects are comparatively small.

The axial velocity derivative in equation (25) can be determined by differentiating a continuity expression:

$$\frac{dV_z}{V_z} = - \frac{dp}{\rho_1} - \frac{da}{A_1} \quad (26)$$

The area derivative in equation (26) is:

$$\frac{da}{A_1} = A_{p*} - 1 \quad (27)$$

and thus (26) becomes

$$\frac{dV_z}{V_z} = - \frac{dp}{\rho_1} A_{p*} + 1 \quad (28)$$

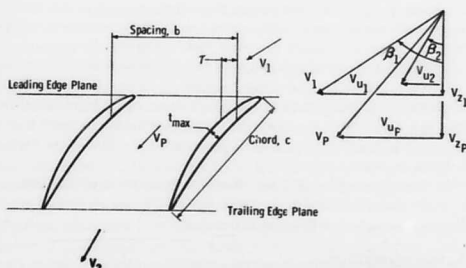


Fig. 15 Sketch showing cascade geometry and nomenclature

The tangential velocity derivative in equation (25) can be evaluated by relating the change in tangential velocity to the overall circulation of the cascade as in equation (17):

$$\frac{1}{2} \frac{dV_u^2}{V_z^2} = \frac{V_{u_1}}{V_{z_1}^2} \Delta V_u = -\frac{V_{u_1}}{V_{z_1}^2} \times \left(K_1 V_1 \sigma \Gamma^* \right) \quad (29)$$

Equations (28) and (29) are substituted into equation (25), which is then used in equation (24) to obtain the following expression for the density in the throat region of the cascade:

$$\frac{\rho_p}{\rho_1} = 1 - \frac{M_z^2}{1 - M_z^2} \left(1 - A_p^* - K_1 \frac{\tan \beta_1}{\cos \beta_1} \sigma \Gamma^* \right) \quad (30)$$

Finally, the ratio of throat velocity to inlet velocity is obtained from equations (17) and (22):

$$\begin{aligned} \frac{V_p}{V_1} &= \left[\left(\frac{V_{u_p}}{V_1} \right)^2 + \left(\frac{V_{z_p}}{V_1} \right)^2 \right]^{1/2} \\ &= \left[(\sin \beta_1 - K_1 \sigma \Gamma^*)^2 + \left[\frac{\cos \beta_1}{A_p^* (\rho_p / \rho_1)} \right]^2 \right]^{1/2} \end{aligned} \quad (31)$$

where:

$$A_p^* = \left[1 - K_2 \sigma \frac{t_{\max}}{c} / \cos \beta \right] \left(1 - \frac{A_{a_1} - A_{a_2}}{3 A_{a_1}} \right)$$

with ρ_p / ρ_1 , given by equation (30) and Γ^* given by equation (18).

In the second term in equation (16), V_{\max}/V_p , the maximum suction surface velocity will be greater than the passage velocity due to blade circulation and the effect of surface curvature. The surface curvature depends in part on blade thickness. Thus, it is proposed that the maximum suction surface velocity: passage velocity ratio can be expressed as:

$$\frac{V_{\max}}{V_p} = 1 + K_3 \frac{t_{\max}}{c} + K_4 \Gamma^* \quad (32)$$

where K_3 and K_4 are empirical constants to be determined.

The third term in equation (16), $V_1/V_{0_{TE}}$, is determined from the cascade inlet and exit vector diagrams.

The four empirical constants were determined as follows. It was observed that all are contained in the first two velocity ratios in equations (16), and that the product of these two velocity ratios is V_{\max}/V_1 . Since V_{\max} can be accurately calculated for two-dimensional incompressible cascades at smooth-flow incidence through the use of an Isay-Martensen-type potential flow analysis, such calculations were made for an array of thirty-four cascades covering a range of solidity from 0.5 to 2.0, a range of stagger from 5 to 67 deg, a range of camber from 0 to 60 deg, and a range of max thickness/chord ratio from 0.03 to 0.15. The resulting V_{\max}/V_1 ratios varied from 1.07 to 1.53. These data were analyzed by a computer program that determined the values of the K coefficients that minimized the RMS deviation between the V_{\max}/V_1 data and the values calculated from the product of equation (31) and (32). A correlation having a RMS deviation of ± 1.8 percent was obtained for values of the constants as given in the following:

$$K_1 = 0.2445$$

$$K_2 = 0.4458$$

$$K_3 = 0.7688$$

$$K_4 = 0.6024$$

The resulting expression for $V_{\max}/V_{0_{TE}}$ is believed to be valid for blade rows operating at an appropriate design incidence angle,

provided that the airfoils are reasonably well shaped for their design conditions. Cases where the flow is compressible up to high subsonic Mach numbers are believed to be represented adequately as long as surface shocks strong enough to cause large separations of the boundary layer are avoided, and meridional Mach numbers are held low enough to prevent blade thickness blockage of the annulus from distorting the flow pattern as might occur if the passage throat were choked.

APPENDIX 2

Some Notes on Surface Finish and Its Effects on Compressor Performance

A short literature survey has been made in an attempt to establish how airfoil surface finish affects compressor performance. A formula relating profilometer readings to Nikuradse sand roughness is proposed, and a value for roughness Reynolds number below which the airfoils can be considered hydraulically smooth is tentatively recommended. It is observed that more research is needed on high-Reynolds-number compressor stages.

Roughness Specification and Measurement. Manufactured parts, such as compressor blades, have roughness specified in microns or microinches. According to the surface finish standard published by ASME (reference [28]) the "roughness height is rated as the arithmetical average deviation expressed in microinches measured normal to the center line." This is the definition that is commonly used on drawings and, unless there is knowledge to the contrary, it should be assumed that roughness-measuring profilometers read this type of roughness. Appendix A of [28] suggests that many roughness measuring instruments are calibrated for root-mean-square average, and that such an instrument will be found to read approximately 11 percent higher on a given surface than one calibrated for arithmetical average. This is apparently based on the fact that a sine wave has 11 percent difference between these averages. For a straight-line saw-tooth function this difference is 15.5 percent. Analysis of stylus traces from sandpaper samples indicate differences varying from 17 to 28 percent.

Arithmetical average will be denoted by the subscript CLA, which stands for centre-line average, because in British literature it is called that. Root-mean-square average will be denoted by RMS.

Equivalent Sand Roughness. In fluid mechanics, roughness is usually specified in terms of an equivalent sand grain size, k_s , employed by Nikuradse [29] in his classical roughness experiments. It is, therefore, necessary to relate sand roughness to the surface finish specifications on drawings and the roughness measurements made on manufactured parts to show compliance with the drawings. Since profilometer-type traces of Nikuradse's actual test surfaces do not seem to be available, the CLA roughness he used must be deduced by other means. The best means so far discovered by the authors is through the measurements of Speidel [30], who determined the k_s values of several standard sandpapers from his own fluid dynamic measurements, with the following results:

ASTM Paper No.	Equivalent		
	Mean grit particle dia k , microns	sand roughness k_s , microns	k_s
320	40	60	1.50
220	60	100	1.67
100	140	180	1.29
80	180	280	1.56
60	250	420	1.68
40	400	580	1.45

Speidel, apparently, did not obtain profilometer traces for his test sandpapers, but other workers have measured such papers. The following table is adapted from Nece and Daily [31]:

ASTM Paper No.	Mean grit particle dia k, microns	Arithmetical avg. roughness k_{CLA} , microns	RMS roughness k_{RMS} , microns	k_{CLA} k
180	79	18	23	0.23
120	124	27	33	0.22
60	250	67	79	0.27

Recent unpublished profilometer analyses by M. R. Brown of General Electric are in reasonable agreement with these measurements.

Taking 1.5 as a representative value for k_s/k , and 0.24 for k_{CLA}/k ,

$$k_s = 6.2 k_{CLA} \quad (33)$$

is obtained.

Equation (33) is in reasonable agreement with the research results of Young [32], who deduced the equivalent sand roughness sizes of camouflage paints by relating the measured drags of painted airfoils to the generalized Nikuradse data. Profilometer traces of the tested paints were also obtained, and the roughness was expressed in terms of a mean roughness height, k_s , obtained by measuring the normal height from trough to crest for each excrescence on a profilometer record and averaging the measurements. He found that k_s was approximately equal to 1.6 k . This can be related to k_{CLA} as follows. If the excrescences were sinusoidal in shape, k would be πk_{CLA} , but if they were sharp like linear saw teeth, k would be $4 k_{CLA}$. This places the coefficient in equation (33) in the range between 5.0 and 6.4, which can be considered reasonable agreement.

Application to Compressor Blading. Schlichting [33] suggests that for roughened flat plates in fully turbulent flow, the surface is hydraulically smooth when the roughness Reynolds number Re_k , based on free-stream velocity and equivalent sand roughness, is less than or equal to 100. Flow conditions in operating compressors may be rather different from those upon which this relation is based in that strong pressure gradients may be present, the blade boundary layers may be partly laminar, and the flow may be quite unsteady. It is, therefore, desirable to examine any test data that may be available to help determine a permissible roughness Reynolds number for compressors.

A partial answer can be obtained from the cascade tests of Bammert and Milsch [34]. These tests, conducted at low speed on sand-roughened NACA 65-Series blades with typical axial-flow compressor staggers, cambers, and solidities, confirmed that the permissible roughness Reynolds number is around 100. Beyond about 100, the losses increase very rapidly with increasing roughness. For these tests the chord Reynolds number was 430,000, and the blade boundary layers were observed to be laminar over approximately the first 50 percent chord, even at roughness Reynolds numbers over 1000.

The authors have not been able to find any directly applicable quantitative data on the effects of airfoil roughness on the performance of an actual compressor. The Mamba research compressor

tests [35] do show some significant effects of roughness but the roughness magnitude is not given. It now appears that the "rough" cast blades tested in the NGTE 106 Compressor [36] were really hydraulically smooth,² and the performance loss was caused by flashing from the casting process and unworked fillets. Two of the three surface finishes tested by Moses and Serovy [37] were hydraulically smooth, and the third was dominated by chordwise grooves that are not representative of current manufacturing practices. Based on upstream relative velocity and using equation (33), the chordwise roughness Reynolds number was about 65 at 80 percent speed and 90 at 125 percent speed, but based on spanwise roughness these values were about three times as large. Performance measurements showed these blades to be about 4 points poorer in efficiency than the smooth blades at 80 percent speed, but no poorer at 125 percent speed and no poorer near stall at any speed. It can be speculated that the blade losses at 125 percent speed and near stall were due more to form drag than skin friction, and that the roughness somehow helped to energize weak boundary layers.

Perhaps, the most meaningful data discovered are from the centrifugal pump tests reported by Nixon and Cairney [38]. After examining data taken over a range of Reynolds number from pumps with different surface finishes and from small and large pumps of the same design, they conclude that the permissible roughness Reynolds number is about 25. However, this surprisingly low value appears to result from their use of the value 1.7 for the coefficient in equation (33) rather than 6.2 when determining roughness from their profilometer readings. If 6.2 were used, their data would give about 90 for the permissible roughness Reynolds number.

Since it is believed that the boundary layers on compressor blades are laminar near the leading edge (and perhaps back to the suction peak or beyond) it is necessary to inquire whether roughness might affect transition even though the airfoil is hydraulically smooth according to turbulent boundary layer criteria. It appears that this is not the case, however, at least for roughnesses that are more or less uniform. Schlichting states [39] that for distributed roughness elements the position of the transition point does not vary because of the roughness as long as the roughness Reynolds number is less than 120, and that this limit is largely independent of whether a pressure gradient is present or not. The data of Bammert and Milsch [34] indicate that for roughnesses several times this great the transition point is not moved forward very much. Their data also suggest that roughness increases the momentum thickness growth of the laminar part of the boundary layer in much the same way that it affects the turbulent boundary layer.

Based on these findings, for the present model, equation (33) has been adopted to relate profilometer readings with equivalent sand roughnesses, and the criterion for hydraulic smoothness is taken as

$$\frac{V_1 k_s}{\nu} \leq 90 \quad (34)$$

where V_1 is the inlet relative velocity, k_s is the equivalent sand roughness, and ν is the kinematic viscosity. Additional research on compressor stages is needed to better establish equation (34), particularly at the high chord Reynolds number values that are typical of large compressor operation.

² Using k_s obtained from equation (33) and the profilometer trace given, the highest roughness Reynolds number tested was 45.